University of California

Ernest O. Lawrence Radiation Laboratory

INTERSTITIAL ORDERING OF CARBON IN TANTALUM

TWO-WEEK LOAN COPY

This is a Library Circulating Copy which may be borrowed for two weeks. For a personal retention copy, call Tech. Info. Division, Ext. 5545

Berkeley, California

DISCLAIMER

This document was prepared as an account of work sponsored by the United States Government. While this document is believed to contain correct information, neither the United States Government nor any agency thereof, nor the Regents of the University of California, nor any of their employees, makes any warranty, express or implied, or assumes any legal responsibility for the accuracy, completeness, or usefulness of any information, apparatus, product, or process disclosed, or represents that its use would not infringe privately owned rights. Reference herein to any specific commercial product, process, or service by its trade name, trademark, manufacturer, or otherwise, does not necessarily constitute or imply its endorsement, recommendation, or favoring by the United States Government or any agency thereof, or the Regents of the University of California. The views and opinions of authors expressed herein do not necessarily state or reflect those of the United States Government or any agency thereof or the Regents of the University of California.

Submitted to Physicus Status Solidi

UCRL-11782 Rev.

UNIVERSITY OF CALIFORNIA
Lawrence Radiation Laboratory
Berkeley, California

Contract No. W-7405-eng-48

INTERSTITIAL ORDERING OF CARBON IN TANTALUM

R. E. Villagrana and G. Thomas

February 1965

INTERSTITIAL ORDERING OF CARBON IN TANTALUM

R. E. Villagrana and G. Thomas*

Department of Mineral Technology, College of Engineering,
University of California, Berkeley, California

ABSTRACT

The effect of interstitial carbon on the structure of tantalum was investigated by transmission electron microscopy and diffraction. Interstitial ordering was found, and the ordered structure was determined from computation and comparison with electron diffraction data. The superlattice structure is tetragonal, with a $\frac{c}{a}$ ratio of 1.128, and an ideal composition of $Ta_{64}C$.

Since the superlattice was determined from thin foils, it was necessary to compare the thin foil results with bulk specimens, alloyed to correspond to $Ta_{64}C$. Microscopic examination of bulk specimens showed many domain boundaries, separating regions in which the tetragonality associated with ordering was oriented in different directions. An analysis of these domain boundaries indicates that there are three possible types: coherent, semicoherent, and antiphase.

*On leave 1964-65 in the Miller Institute for Basic Research, University of California, Berkeley, California.

1. INTRODUCTION

Although macroscopic studies have been made of the physical properties of solid solutions of interstitial solutes, such as H, C, N, O in the Group VB body-centered cubic metals, little is known about the microstructure of these alloys. As mechanical properties are strongly structure dependent, an understanding of the behavior of these alloys necessitates a knowledge of the structure under investigation. In the past two years, evidence has been obtained by transmission electron microscopy which suggests that the interstitials occupy preferred sites, resulting in "interstitial ordering."

The use of x-ray diffraction to study such ordering is limited by the relatively low scattering power of the interstitial elements (H, C, N, O), and because relatively large volumes of crystal are irradiated. As electron diffraction intensities are about 10^4 times greater than those of x-rays, and because selected area diffraction can be done on relatively small volumes of crystal ($\sim 1\ \mu^3$), detection of interstitial ordering is more likely by electron diffraction than by x-ray diffraction. Therefore, transmission electron microscopy studies coupled with selected area diffraction techniques present an excellent means for structure analysis of these systems which would be difficult, if at all practical, with conventional x-ray diffraction techniques.

In an investigation of the effect of interstitial N in Ta, Seraphim et al.[1] were the first to attempt to correlate transmission electron microscopy observations with interstitial ordering in the Group VB metals. Seraphim et al. proposed an ordered structure $Ta_{27}N$

on the basis of x-ray Weissenberg camera investigations. Van Torne and Thomas [2], and more recently Van Landuyt [3], have made detailed electron microscopy studies on the phase transformation induced by interstitial O in Nb. These workers observed that ordering followed by a definite phase transformation to FCC NbO occurred. With the aid of hot stage microscopy and ciné techniques, Van Torne and Thomas were able to determine the temperature at which the transformation occurs. Ordering of interstitial hydrogen in tantalum [4] has also been suggested, but so far the structures of the ordered alloys have not been reported.

In this investigation the effect of interstitial carbon (up to 2.94 at. %) on the structure of tantalum was studied by transmission electron microscopy and diffraction.

2. EXPERIMENTAL PROCEDURE

2.1 Specimen Preparation

High purity single crystals, 0.6 cm diameter by 10 cm in length, were grown in an electron-beam zone refiner from commercial tantalum rod stock. Specific resistivities were measured (the ratio from liquid He to room temperature was 10^4), and from these data the ratio of interstitial impurities to tantalum atoms were calculated [5] to be 10^{-9}. The single crystals were carefully rolled into strips 6 - 10 mils in thickness, washed with methyl alcohol, and annealed at 1300°C for 5 hours in dynamic vacuum of approximately 10^{-6} mm Hg. At this point foils were examined in the electron microscope to determine if any ordering transformation had occurred due to possible impurity pickup, or if any transformation could be induced. In no case was any transformation detected, nor could any transformation be induced by beam

heating in the microscope. This implies that the impurity pickup was negligible during the rolling and annealing operations.

After annealing, the tantalum strips were cleaned by dipping in hydrofluoric acid (48%), and then washed with methyl alcohol. At all stages extreme caution was exercised in the handling of the strips in order to avoid contamination.

The clean tantalum strips were weighed on a Mettler type BC 1000 substitution balance to an accuracy of ± 0.1 mg. They were then transferred to a vacuum evaporator, where a thin film of carbon was deposited on one surface of the metal. The specimens were then placed in the vacuum furnace, and the carbon allowed to diffuse into the tantalum at various times and temperatures. After treatment, the specimens were removed and reweighed, the difference in weight being equal to the amount of carbon taken up by the tantalum. Table I summarizes the carbon content, and the various heat treatments for each specimen.

TABLE I

At. % Carbon	Annealing Temp. °C	Annealing Time Hr.	Vacuum mm Hg.
1.54	1000	24	$\simeq 10^{-6}$
1.82	1000	48	$\simeq 10^{-6}$
2.28	1300	24	$\simeq 10^{-6}$
2.94	1500	24	$\simeq 10^{-6}$

2.2 Preparation of Electron Transparent Foils

Thin foils suitable for transmission electron microscopy were prepared by chemical polishing in a solution of 50 vol. % hydrofluoric

acid and 50 vol. % nitric acid. The specimens were held in the polishing solution for five minutes, washed with methyl alcohol to remove surface films, then replaced.

While polishing, the specimen was periodically examined with an optical microscope. If etching was detected then the polishing solution was altered by the addition of more nitric acid.

2.3 Microscopic Investigation

Transmission electron microscopy and selected area diffraction investigations were done in the usual way in a Siemens Elmiskop 1 electron microscope.

The Ta-C specimens were first examined in the microscope under conditions in which the transformation could occur during observation. The transformation was induced by regulating the electron beam to heat the foil. This procedure offered more control over the reaction rate than pulse heating (removal of the condenser aperture).

Observations on bulk specimens, which had been transformed outside the microscope, were made using the double tilt specimen stage. This was necessary to investigate the nature of the contrast and to facilitate interpretation of the diffraction patterns.

3. THIN FOIL RESULTS AND INTERPRETATION

3.1 Microscopic Observations

As reported by Van Torne and Thomas [2], and Van Landuyt [3] for NbO, the thin foil ordering transformation observed in the present work occurred in two distinct steps. As a result of heating by the electron beam, thin regions of the foil were observed to transform with the simultaneous formation of discrete nuclei, whose habit planes were {110}.

An example is shown in Fig. 1. This nucleation process was observed to take place homogeneously, probably due to carbon composition fluctuations in the thin refions of the foil. These small domains then grew until they impinged, as shown in Fig. 2.

The final stage of the ordering transformation occurred with the formation of highly ordered regions separated by coherent and antiphase domain boundaries. The transition period from impingement to the highly ordered final stage is shown in Fig. 3. The final stage of the transformation is shown in Fig. 4. In Fig. 4 the boundaries at A and B are coherent domain boundaries (the nature of these boundaries will be discussed in the next section) on $(1\bar{1}0)$ and (110), respectively. At C the boundaries are primarily {210} antiphase domain boundaries.

The transformation does not always proceed in this manner, but sometimes appears to be, subject to the morphology of the tantalum surface, e.g. in Fig. 5a, b, c. The transformation in Fig. 5a has not quite gone to completion, as the diffraction pattern showed only the initial stages of superlattice formation.

3.2 Structure Determination of $Ta_{64}C$

From selected area diffraction patterns obtained in regions similar to that of Fig. 4 it became apparent that an ordering process had taken place. This was deduced because, besides the primary tantalum diffraction pattern, there was also the superposition of a second, smaller spaced, diffraction pattern corresponding to a superlattice structure. The problem is to construct from the superlattice diffraction pattern the superlattice unit cell. Because of the inherent difficulties in correlating intensity calculations with selected area diffraction data,

a variation of the algebraic methods described by Vainshtein [6] were utilized. Using such algebraic methods it is only possible to derive geometric structures, and not precise atomic coordinates. A model was constructed whose associated structure factor accounted for all superlattice reflections either present or absent. The actual structure determination involved the analysis of many selected area diffraction patterns, and trial and error attempts to construct a model compatible with these diffraction data. The diffraction pattern associated with Fig. 4 is enlarged and shown in Fig. 6a. This pattern contains enough data to illustrate how the structure was determined.

Figure 6a shows a [001] BCC tantalum pattern tilted slightly about [200], with a superlattice diffraction pattern superimposed. In this diffraction pattern first order superlattice relpoints are spaced parallel to $(1\bar{1}0)_{BCC}$ and $(110)_{BCC}$ relpoints at a distance of $1/4\ (\bar{g}_{110})_{BCC}$. This implies that in real space there are superlattice planes parallel to $\{110\}_{BCC}$ at a d spacing four times that of $(110)_{BCC}$. Similarly, there are first order superlattice planes parallel to $\{200\}_{BCC}$ each at a d spacing four times that of $(200)_{BCC}$. Considering these facts, it is concluded that the superlattice unit cell should be approximately equal to four a_o on edge, where a_o is the lattice parameter for BCC tantalum. It is next necessary to locate the positions of the carbon atoms in relation to the superlattice unit cell (defined by tantalum atoms).

The basic structure factor equation for unit cells containing n atoms of the same kind can be written

$$F_{hk\ell} = \sum_{1}^{n} f_n\, e^{2\pi i\,(hx_n + ky_n + \ell z_n)} \qquad \text{Eq. 1}$$

where f_n is the atomic scattering factor, $(hk\ell)$ the Miller indices, and $(x_n\ y_n\ z_n)$ the atomic coordinates. The indicated sum is carried out over the unit cell under consideration. For the superlattice structure, $F_{hk\ell}$ will be a function of both tantalum atoms and carbon atoms, and so Eq. 1 is now written in the form

$$F_{hk\ell} = f_{Ta} \left[\sum_{1}^{n} e^{2\pi i\ (hx_n + ky_n + \ell z_n)}\right] + f_C \left[\sum_{1}^{j} e^{2\pi i\ (hx_j + ky_j + \ell z_j)}\right] \qquad \text{Eq. 2}$$

The tantalum terms have already been tentatively determined by the choice of superlattice cell size. Therefore, carbon atoms must be added in varying positions until a structure factor is obtained which is compatible with all the diffraction data. Since the structure factor is quite large, due to the many tantalum terms, it was convenient to utilize an IBM 7094 computer in solving the various structure factors. After numerous attempts, the structure factor which was consistent with all the diffraction data was determined to be

$$F_{hk\ell} = f_{Ta}\ [T] + f_C\ [C] \qquad \text{Eq. 3}$$

where $T = \sum_{x=o}^{3} \sum_{y=o}^{3} \sum_{z=o}^{3} e^{2\pi i\ (\frac{hx}{4} + \frac{ky}{4} + \frac{\ell z}{4})} + \underbrace{\sum_{x=1}^{7} \sum_{y=1}^{7} \sum_{z=1}^{7}}_{\text{odd integers}} e^{2\pi i\ (\frac{hx}{8} + \frac{ky}{8} + \frac{\ell z}{8})}$

and $C = e^{2\pi i\ (\frac{k}{8})} + e^{2\pi i\ (\frac{h}{2} + \frac{5k}{8} + \frac{\ell}{2})}$.

In Eq. 3 the f_C terms correspond to a body-centered arrangement of carbon atoms. The selection rules predicted by Eq. 3 are the same as those for the body-centered space lattice, viz., $h + k + \ell$ even for reflections present, and $h + k + \ell$ odd for reflections absent.

Figure 7 shows the superlattice; the spheres represent carbon atoms in $0\frac{1}{2}0$ octahedral positions and the squares are BCC tantalum unit cells. The superlattice corresponds to an ideal composition of $Ta_{64}C$. A hard sphere model, similar to Fig. 7, shows that by placing carbon atoms in $0\frac{1}{2}0$ type positions an expansion in the [010] direction, and a slight contraction in the [100] and [001] directions must occur. Therefore, the superlattice unit cell is tetragonal. The tetragonality was confirmed in <100> patterns because a definite, but slight, contraction of one of the $(\bar{g}_{200})_{BCC}$ vectors, and a corresponding change in the angle between $(\bar{g}_{110})_{BCC}$ vectors was observed. These observations show that the $\frac{c}{a}$ ratio cannot be unity.

3.3 Superlattice Pattern Indexing

Figure 6b shows the indexed superlattice diffraction pattern using the selection rules predicted by Eq. 3. Only the strong first and second layer relpoints of Fig. 6a are indexed. To index this pattern the tantalum indices must be transposed to superlattice indices as predicted by the structure factor equation. The following expression, utilizing a similarity matrix, can be used to make this transformation.

$$\begin{Vmatrix} h \\ k \\ \ell \end{Vmatrix}_S = \begin{Vmatrix} 4 & 0 & 0 \\ 0 & 4 & 0 \\ 0 & 0 & 4 \end{Vmatrix} \begin{Vmatrix} h \\ k \\ \ell \end{Vmatrix}_{Ta} \qquad \text{Eq. 4}$$

Care must be taken in using Eq. 4, for in some cases the BCC tantalum relpoint might be tilted off the reflecting sphere, and the corresponding second layer superlattice relpoint tilted onto the reflecting sphere. It is thus very important to tilt the foil into exact orientation to avoid difficulties in indexing. As the structure is tetragonal, it is

necessary to know the $\frac{c}{a}$ ratio in order that reasonable angles and d spacings can be calculated. The $\frac{c}{a}$ ratio was determined from Kikuchi lines (section 4, 4.4) to be 1.128.

4. BULK SPECIMEN RESULTS AND INTERPRETATION

4.1 Microscopic Observations

As the superlattice structure in Fig. 7 was determined on the basis of thin foil observations, it was necessary to compare the thin foil behavior with that of bulk specimens. The composition of the ordered structure is $Ta_{64}C$, the bulk specimen alloyed to correspond to this composition contained 1.54 at. % C(see Table I) or a composition $Ta_{66}C$. Microscopic examination of this specimen, Fig. 8, showed a multitude of domain boundaries similar to those reported for impure Nb[7] and Ta[8].

The domain boundaries were observed to be highly mobile under the heating effect of the electron beam. This made microscopic examination difficult, as low beam currents caused the domain boundaries to migrate, and subsequently disappear. These domain boundaries move presumably because of the easy diffusion of interstitial carbon atoms. Upon lowering the beam current, the boundaries returned to approximately their initial positions, but the contrast from the boundaries was not as sharp, nor could tilting bring the boundaries into better contrast.

It was also observed that some domain boundaries were more resistant to beam heating than others. In virtually all cases these boundaries were found to be on or near {110}.

4.2 Contrast from Domain Boundaries

A detailed dynamical theory explaining the contrast from domains,

and the basic crystallographic conditions necessary for contrast, have been developed by Gevers et al. [9,10]. Consider a thin foil, as in Fig. 9, which is separated into two regions by a domain boundary. Furthermore, let the two crystals be tetragonal with c axes oriented normal to each other as shown in Fig. 9, resulting in [001] being the orientation of crystal I and [010] the orientation of crystal II. In effect, the domain boundary divides the crystal into two wedged segments, with the crystal structure differing slightly in dimension in each segment. This slight difference in crystal structure appears in selected area diffraction patterns taken across domain boundaries. In Fig. 9, crystal I gives a four fold symmetrical cubic diffraction pattern, and crystal II gives a two fold tetragonal diffraction pattern. The superposition of these two diffraction patterns results in pairing of the Kikuchi lines and higher order relpoints. The contrast associated with a boundary arises from three sources (i) differences in extinction distances for reflections of the same indices in each segment (ii) a change in the phase angle at the boundary (iii) the diffraction conditions in crystal I differ from those in crystal II, resulting in a difference in the deviation parameter s on either side of the domain boundary.

The fringe patterns associated with domain boundaries are different from those of stacking faults, or twin boundaries. In bright field the first and last fringes from domain boundaries are asymmetrical, and in dark field they are symmetrical with respect to the fringe at the surface of the foil in bright field [9,10]. This is shown in Fig. 10a,b.

As the angle ϕ in Fig. 9 approaches zero the boundary disappears, and as ϕ approached 90 degrees the boundary appears as a line separating

regions of opposite contrast. The latter case is visible in regions A and B of Fig. 4 for the {110} boundaries.

In Figs. 8 and 10 the domain boundaries are overlapping. The nature of the contrast effects in the central portions of these overlapping fringes are similar to the three cases of overlapping stacking faults in rutile [11]. The three possible configurations for overlapping domain boundaries are shown in Fig. 11, and all three types are present in Fig. 8.

The overlapping domain boundaries in Fig. 10 show an interesting contrast effect. In Fig. 10 the boundaries appear to be type I (see Fig. 11), but the dark field image does not show the contrast expected for type I boundaries (the extreme fringes appear to be asymmetrical). Actually, the boundaries are type II, as indicated at A and B in Fig. 10a,b. The region of overlap of two domain boundaries can show three types of contrast: dark, light, or fringes. The nature of the contrast in the region of overlap depends on the relative separation of the two domain boundaries.

The domain boundaries in Fig. 10 show a definite change in contrast in the overlap region (except for the extreme fringes). This change in contrast indicates that the distance between overlapping domain boundaries is constantly changing. The changing distance between domain boundaries indicates that the boundaries are not rigidly confined to a crystallographic plane. This conclusion is confirmed by observations of boundaries making large angles ($\phi \approx 90°$) to the foil surface such as in Fig. 12.

4.3 Crystallography of Domain Boundaries

From the diffraction geometry associated with domain boundaries [10], and trace analysis [12], it is possible to determine the plane of the boundary. This was done for Fig. 8. If the conditions for observing domain boundary contrast are met and the plane of the boundary is known, it is possible to construct a boundary model based on the superlattice structure. When this was done, it was found that the resulting domain boundaries could be classified into three general types: coherent, semicoherent, or antiphase.

The coherent domain boundary is defined by a {110} plane, and is energetically the most stable. This type of boundary is shown in Fig. 13 as a (110) plane in edge view (in all the diagrams, squares represent tantalum unit cells, and circles carbon atoms). On one side of this boundary the atoms are pictured as open circles in $\frac{1}{2}00$ octahedral positions, and on the other side as shaded circles in $0\frac{1}{2}0$ octahedral positions. The resulting tetragonality is as indicated in the upper diagram in Fig. 13. The formation of the boundary in Fig. 13 can be described by the following shift involving the carbon atoms on one side of the (110) plane only.

$$\frac{a_s}{2}\langle 100\rangle + \frac{c_s}{2}\langle 100\rangle + \frac{a_o}{2}\langle 110\rangle$$

where a_s and c_s are the lattice parameters of the tetragonal superlattice, and a_o is the lattice parameter of the BCC tantalum. Positions 2 and 4 in Fig. 13 define coherent domain boundaries. The reaction for these positions would be

$$\text{Position 2} = \frac{a_s}{2}[010] + \frac{c_s}{2}[\bar{1}00] + \frac{a_o}{2}[110]$$

or

$$\text{Position 4} = \frac{a_s}{2}[010] + \frac{c_s}{2}[\bar{1}00] + \frac{a_o}{2}[\bar{1}\bar{1}0]$$

In the coherent domain boundary the tetragonal c axes are coupled (intersect at the same point on the boundary), and the carbon atoms are in twin relationship about the (110) plane (the carbon atoms are mirrored about the domain boundary). For position 4 the boundary is as indicated in Fig. 13, but for position 2 the boundary should be shifted up.

Positions 1 and 3 in Fig. 13 describe the semicoherent domain boundary. The same general reaction that was used in describing the coherent domain boundary can be used in describing the semicoherent domain boundary in Fig. 13. The two positions can be described by the following shifts

$$\text{Position 1} = \frac{a_s}{2}[010] + \frac{c_s}{2}[\bar{1}00] + \frac{a_o}{2}[\bar{1}10]$$

or

$$\text{Position 3} = \frac{a_s}{2}[010] + \frac{c_s}{2}[\bar{1}00] + \frac{a_o}{2}[1\bar{1}0]$$

In this type of boundary the tetragonal c axes are coupled, but the carbon atoms are not mirrored about the (110) boundary plane. Once again, the boundary is drawn correctly for position 1, but should be shifted up for position 3.

The antiphase domain boundary is energetically the most unstable, and is not confined to any particular crystallographic plane. A (111) antiphase domain boundary is shown in Fig. 14. This domain boundary can be produced by a simple $\frac{1}{2}$ a_o <110> translation of carbon atoms on one-half of the boundary to opposite octahedral sites, without changing

the carbon atom positions on the other side of the boundary. Figure 14 illustrates four possible positions. In this type of boundary there is no head to tail coupling of the tetragonal c axes, and the carbon atoms are not mirrored about the (111) plane.

In the previous section it was shown that domain boundaries are not necessarily confined to a particular crystallographic plane (e.g. Fig. 12). Thus, the type of boundary (coherent, semicoherent, or antiphase) can vary since its plane may change along the length of the boundary.

4.4 Determination of the $\frac{c}{a}$ Ratio for $Ta_{64}C$

As discussed earlier, the diffraction patterns taken across domain boundaries showed a pairing of the relpoints, and the associated Kikuchi lines. It is possible to estimate the $\frac{c}{a}$ ratio for the superstructure from these paired relpoints, but for a more accurate ratio, Kikuchi lines should be utilized [13,14].

Figure 15 is a diagram of reciprocal space in [001] orientation. Consider an arbitrary relpoint, say the (210) cubic (this reflection is not an allowed BCC reflection, but is shown for convenience), and introduce some tetragonality along the [100] axis. The $(210)_C$ cubic relpoint now becomes the $(210)_T$ tetragonal relpoint. In the case of domain boundaries, both the paired cubic and tetragonal relpoints are visible for higher order reflections. In Fig. 15, the angle between the [100] axis and the $(210)_C$ relpoint is θ, and the angle between the $(210)_C$ relpoint and the $(210)_T$ relpoint is $\Delta\theta$. Therefore, the angle between the $(210)_T$ relpoint and the [100] axis is α, where $\alpha = \theta + \Delta\theta$.

By substituting α into the equation for the angle between two planes in the tetragonal system,

$$\cos\alpha = \frac{\dfrac{h_1 h_2 + k_1 k_2}{a^2} + \dfrac{\ell_1 \ell_2}{c^2}}{\left[\left(\dfrac{h_1^2 + k_1^2}{a^2} + \dfrac{\ell_1^2}{c^2}\right)\left(\dfrac{h_2^2 + k_2^2}{a^2} + \dfrac{\ell_2^2}{c^2}\right)\right]^{\frac{1}{2}}} \qquad \text{Eq. 5}$$

it is then possible to solve for the $\frac{c}{a}$ ratio directly.

The problem is to calculate $\Delta\theta$ as accurately as possible; this is done using paired Kikuchi lines. The Kikuchi line associated with a given relpoint is normal to an imaginary line extending from the transmitted beam to the relpoint. Thus, by simple geometry, and as shown in Fig. 15, the paired Kikuchi lines associated with the $(210)_C$ and $(210)_T$ relpoints intersect at an angle $\Delta\theta$. In the general case for paired Kikuchi lines it is necessary to utilize a stereographic projection in determining the angular relationships.

Figure 16a shows the diffraction pattern associated with Fig. 8, and Fig. 16b shows the analysis of this pattern. In determining the $\frac{c}{a}$ ratio the $3\bar{3}2$ paired Kikuchi lines shown in Fig. 16 were used, and the $\frac{c}{a}$ ratio was calculated to be 1.128. The $\frac{c}{a}$ ratio calculated from a hard sphere model similar to Fig. 7 was found to be 1.08, but this ratio is too low because the contraction along the a_s axes was neglected.

5. DISCUSSION

5.1 Thin Foil Observations

The ordering transformation is attributed to the alloyed interstitial carbon, since a pure tantalum foil was subjected to the same treatments as the Ta-C specimens and no transformation could be induced.

Also, during microscopic examination, some deposition of minute traces of carbon or other impurities from the vacuum system probably occurs, but this would only accelerate the ordering transformation. Except when beam heating was purposely done, the spot size, beam current and condenser illumination were adjusted so that the specimen temperature was kept to a minimum ($<100°C$), to ensure minimizing effects from impurities deposited on the specimen during examination.

The ordering reaction has been attributed to composition fluctuations in the thin regions of the foil. The fact that the transformation started in thin regions was verified by many observations; the real question arises as to why it was initially restricted to these areas. Two possible explanations are immediately evident. First, under the influence of beam heating, carbon diffuses throughout the specimen until the ideal ratio of carbon to tantalum (1:64) is achieved in some areas for the transformation to proceed. Statistically, the ideal carbon to tantalum ratio will be obtained first in the thin regions of the foil. The second possibility is that small traces of impurities deposited during microscopic examination diffuse into the specimen. This added influx of carbon would have the effect of speeding up the ordering reaction in the thin regions as the amount of interstitial carbon necessary for the transformation is lowered. When the microscope is operated under normal conditions, the impurity pickup from the vacuum is insufficient to cause the transformation in pure tantalum foils prepared from zone refined crystals.

In all cases, microscopy studies were performed on tantalum specimens alloyed with, previously predicted, solid solution quantities

of carbon. Because the $Ta_{64}C$ superlattice transformation could be induced in all the specimens, the Ta-C phase diagram should be corrected to include this phase. In all the specimens examined the $Ta_{64}C$ structure was the only second phase material detected.

5.2 Determination of $Ta_{64}C$

In deducing the structure from electron diffraction data it is necessary to avoid obtaining second layer relpoints. To ensure this, selected area diffraction patterns should be taken in exact orientation [14]. Only under this condition can meaningful angular and distance relationships be measured. By exact orientation, it is meant that the foil plane (and hence the plane of the reciprocal lattice) is exactly normal to the incident beam.* This orientation is most readily achieved with the use of a double tilt specimen stage. Similarly, for obtaining maximum contrast information from the image, it is best to "gun tilt" into dark field at s close to zero [14]. This ensures maximum contrast as the specimen is now in exact Bragg diffraction conditions with a two beam case operating.

The $Ta_{64}C$ superstructure determined is a trial structure; the actual sites of the carbon atom (octahedral or tetrahedral) were not established. However, the results from the $\frac{c}{a}$ ratio measurements indicate that the positions are octahedral.

*Under these conditions the diffraction pattern is perfectly symmetrical. If the foil is thick, the centers of symmetry of Kikuchi and relpoint patterns coincide [13].

5.3 Bulk Specimen Observations

The observed migration, and subsequent disappearance of a domain boundary during beam heating, can be explained on the basis of a simple order-disorder reaction. The motion of the boundary during beam heating is caused by the diffusion of interstitial carbon. As the temperature of the specimen is raised, the diffusion becomes more rapid and the order in the regions adjacent to the domain boundary may be destroyed. With this destruction of order is coupled the simultaneous disappearance of the domain boundary.

The disappearance of these boundaries by localized heating, sets up an energetically unfavorable situation which, upon lowering the beam intensity, is remedied by the boundary returning to its initial configuration. The reason for the semi-reversibility of this reaction is thought to be associated with internal stress fields set up by neighboring domains that have been unaffected by the heat of the beam.

It was also observed that under the influence of beam heating, some boundaries were more resistant to motion than others. This implies that some boundaries are energetically more stable than others, and therefore, require more energy to dissociate. Although quantitative measurements are difficult to make, the {110} boundary was the last to dissociate in virtually all cases. This is in agreement with the domain boundary models as the {110} domain boundary can be coherent. The coherent domain boundary is energetically the most stable.

The diffraction phenomena associated with domain boundaries are also of interest. In regions with many overlapping domains, similar to Fig. 8, the absence of a coherent superlattice diffraction pattern

is noticed; but, in regions where the domains are more widely spaced, superlattice diffraction patterns were found. This can be explained when one considers the high degree of order necessary to produce a superlattice diffraction pattern. In regions such as shown in Fig. 8, the superlattice diffraction pattern is not reinforced, due to the different diffracting conditions from domain to domain.

6. CONCLUSIONS

1. Tantalum alloyed with less than 3 at. % interstitial carbon, underwent a two-stage interstitial ordering transformation during microscopy examination. The transformation was induced in the thin foil specimen by heating with the electron beam. The first stage is the nucleation of small ordered domains, on {110}, in thin regions of the foil. These small domains then grow, impinge, until the final stage of highly ordered regions is left.

2. The ordered structure was determined from electron diffraction analysis, and corresponded to a composition $Ta_{64}C$. The superlattice unit cell is tetragonal and is shown in Fig. 7.

3. The $\frac{c}{a}$ ratio for the ordered structure was determined from paired Kikuchi lines to be 1.128.

4. Bulk specimens, alloyed to correspond to the composition of the ordered structure, showed a multitude of ordered regions separated by domain boundaries.

5. Three types of domain boundaries are possible based on the ordered structure: coherent, semicoherent, and antiphase.

6. The Ta-C phase diagram should be modified to include the $Ta_{64}C$ ordered phase.

7. The existence of domains in the refractory metals containing interstitials must certainly affect the mechanical properties, e.g., the ductile-brittle transition. The transport properties such as superconductivity may also be related to the domain structure. Experiments are now in progress to investigate the effect of ordering on these properties.

ACKNOWLEDGMENTS

The helpful discussions with Dr. S. Amelinckx are gratefully acknowledged. This work was supported under the auspices of the U.S. Atomic Energy Commission through the Inorganic Materials Research Division of the Lawrence Radiation Laboratory.

REFERENCES

1. D. P. Seraphim, N. R. Stemple and D. T. Novick, J. Appl. Phys., 33, 136 (1962).

2. L. I. Van Torne and G. Thomas, Acta Met., 12, 601 (1964).

3. J. Van Landuyt, Phys. Stat. Sol., 6, 957 (1964).

4. D. Hull and D. C. Wynne, Proceedings of the Third European Congress on Electron Microscopy, Prague, 1964 (Czech. Acad. Sci., Prague, 1964), p. 239.

5. L. I. Van Torne, The Electrical Transport and Mechanical Properties of Tantalum-Molybdenum Alloy Single Crystals (Ph.D. Thesis), UCRL-11752, January 1965.

6. B. K. Vainshtein, Structure Analysis by Electron Diffraction, (Macmillan Co., New York, 1964), p. 212

7. J. Van Landuyt and S. Amelinckx, Appl. Phys., Letters, 4, 15 (1964).

8. L. Stals and J. Van Landuyt, Phys. Stat. Sol. 5, K1 (1964).

9. R. Gevers, P. Delavignette, H. Blank and S. Amelinckx, Phys. Stat. Sol., 4, 383 (1964).

10. R. Gevers, P. Delavignette, H. Blank, J. Van Landuyt, and S. Amelinckx, Phys. Stat. Sol. 5, 595 (1964).

11. J. Van Landuyt, R. Gevers and S. Amelinckx, Phys. Stat. Sol. 7, 307 (1964).

12. G. Thomas, Transmission Electron Microscopy of Metals (John Wiley & Sons, Inc., New York, 1962), p. 273.

13. M. Von Heimendahl, W. Bell, and G. Thomas, J. App. Phys., 35, 3614 (1964).

14. G. Thomas, Trans. AIME (to be published). UCRL Report No. 11751.

Fig. 1 Ta - 2.28 at. %C showing initial stages of ordering induced by beam heating in a thin region of a thick foil. The domain boundary planes are {110}. The foil orientation is approximately [100].

Fig. 2 Ta - 2.94 at. %C showing striations due to ordering on {110}. The striations are domain boundaries which are impinging. The foil orientation is approximately [$\bar{1}$03].

Fig. 3 Ta - 1.82 at. %C showing an intermediate stage of the ordering transformation observed in the microscope. The foil orientation is [$\bar{1}$10].

Fig. 4 Ta - 1.82 at. %C showing the highly ordered, final stage of the transformation. The boundaries at A and B are coherent domain boundaries on (1$\bar{1}$0) and (110), respectively. At C the boundaries are primarily {210} antiphase domain boundaries. Orientation [001].

Fig. 5 (a) Ta - 2.28 at. %C. This specimen shows a different morphology of transformation, probably a result of the initial surface condition of the foil. From the diffraction pattern it appears to be at approximately the same stage of ordering as shown in Fig. 3. The foil orientation is [001]

(b) Dark field image (gun tilt) of the $(110)_{BCC}$ reflection.

(c) Dark field image of the $(420)_S$ reflection.

Fig. 6 (a) Enlarged selected area diffraction pattern of Fig. 4, showing superlattice relpoints.

(b) Analysis of the more prominent relpoints in (a).

Fig. 7 Structure of the superlattice $Ta_{64}C$. The subscript s refers to the superlattice unit cell, where $a_s \cong 4a_o \neq c_s$. The lattice parameter of BCC tantalum is a_o. The tantalum unit cells are shown as squares. The spheres represent carbon atoms in $0\frac{1}{2}0$ octahedral positions, defining a BCT cell.

Fig. 8 Domain boundaries in Ta - 1.54 at. % C after bulk annealing 24 hours at 1000°C. The overlapping domain boundaries at A and B are on $(\bar{1}0\bar{2})$ and $(1\bar{1}\bar{1})$, respectively. Three cases of overlap (see Fig. 11) are circled.

Fig. 9 Schematic diagram showing crystal geometry on either side of domain boundary for contrast.

Fig. 10 (a) Overlapping domain boundaries in Ta - 1.54 at. % C after annealing 24 hours at 1000°C. The foil orientation is approximately [111].

(b) Dark field image (gun tilt) of the $\bar{1}\bar{2}3$ reflection. Note that the extreme fringes of the domain boundary at A and B are asymmetrical in bright field (a), but symmetrical in dark field. This proves that the top of the domain corresponds to the first white fringe for A and the first dark fringe for B.

Fig. 11 Schematic diagram of possible contrast effects from overlapping domain boundaries. In case I the boundaries are not truly overlapping, and there is an obvious contrast difference on either side of each domain boundary. In Fig. 8, the $(1\bar{1}\bar{1})$ domain boundaries show contrast similar to case I, and the $(\bar{1}0\bar{2})$ domain boundaries show contrast similar to cases II and III. The assumed operating $\bar{g}$ for all the cases is to the right.

Fig. 12 Ta - 2.28 at. % C. Many of the domain boundaries are bending, showing that they are not confined to a single plane. Orientation is approximately [001].

Fig. 13 Sketch of coherent and semicoherent domain boundaries. The carbon atoms are shown as circles in octahedral sites, and the tantalum unit cells are squares. Positions 2 and 4 define coherent domain boundaries, and positions 1 and 3 define semicoherent domain boundaries. The tetragonality associated with these boundaries is shown.

Fig. 14 Sketch of a (111) antiphase domain boundary. The upper half of the diagram shows a (111) antiphase domain boundary as seen down the [001] axis. The lower half of the diagram shows the (111) antiphase domain boundary when folded into edge view. The carbon atoms are shown as circles in octahedral positions, and the tantalum unit cells as squares. Four possible positions of the carbon atoms, which would yield a (111) antiphase domain boundary, are indicated. The tetragonality associated with this boundary is shown.

Fig. 15 Diagram of reciprocal space in [001] orientation showing the relationship between paired (210) relpoints and paired (210) Kikuchi lines.

Fig. 16 (a) Enlarged selected area diffraction pattern of Fig. 8 showing paired relpoints and Kikuchi lines.

(b) Analysis of (a).

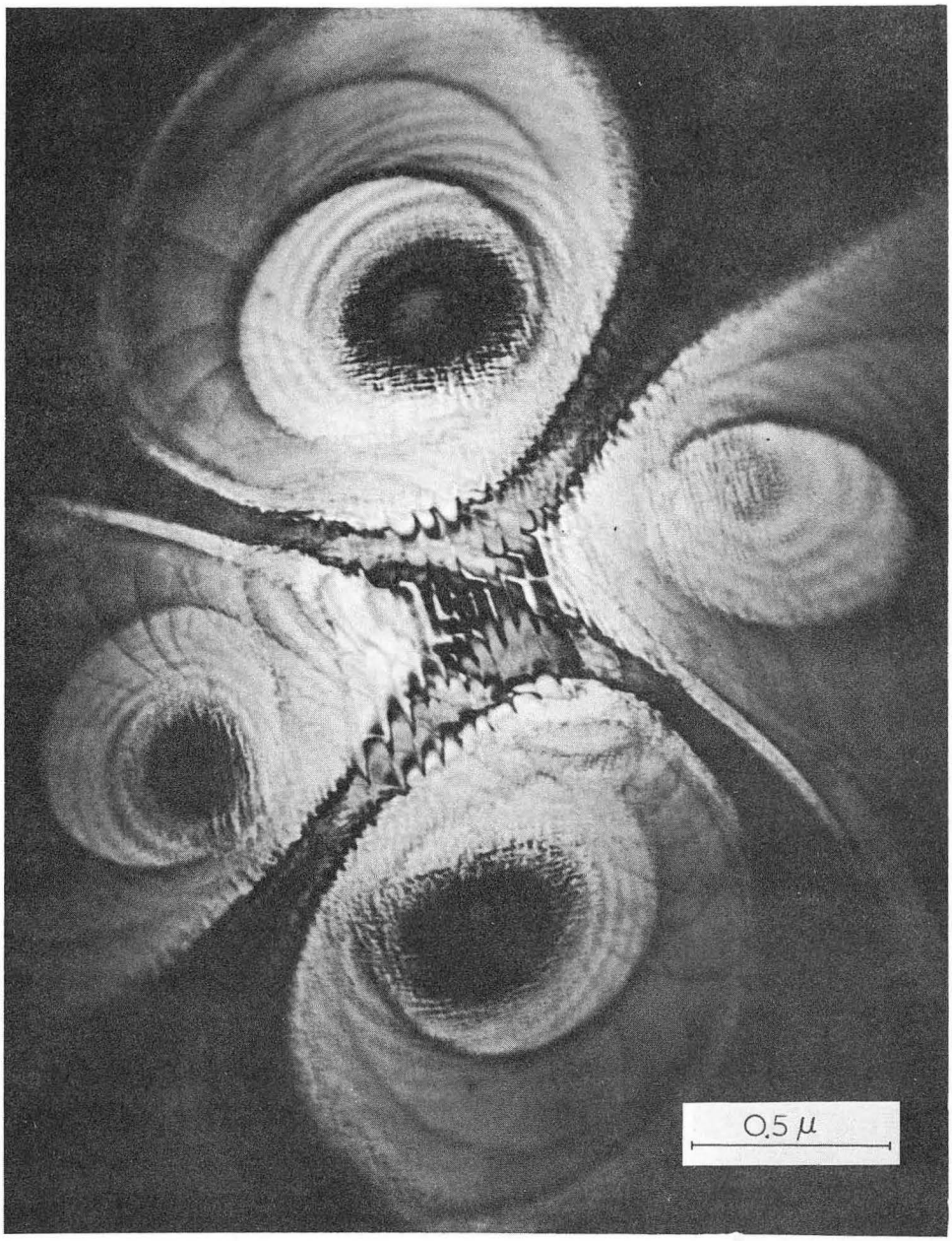

ZN-4716

Fig. 1

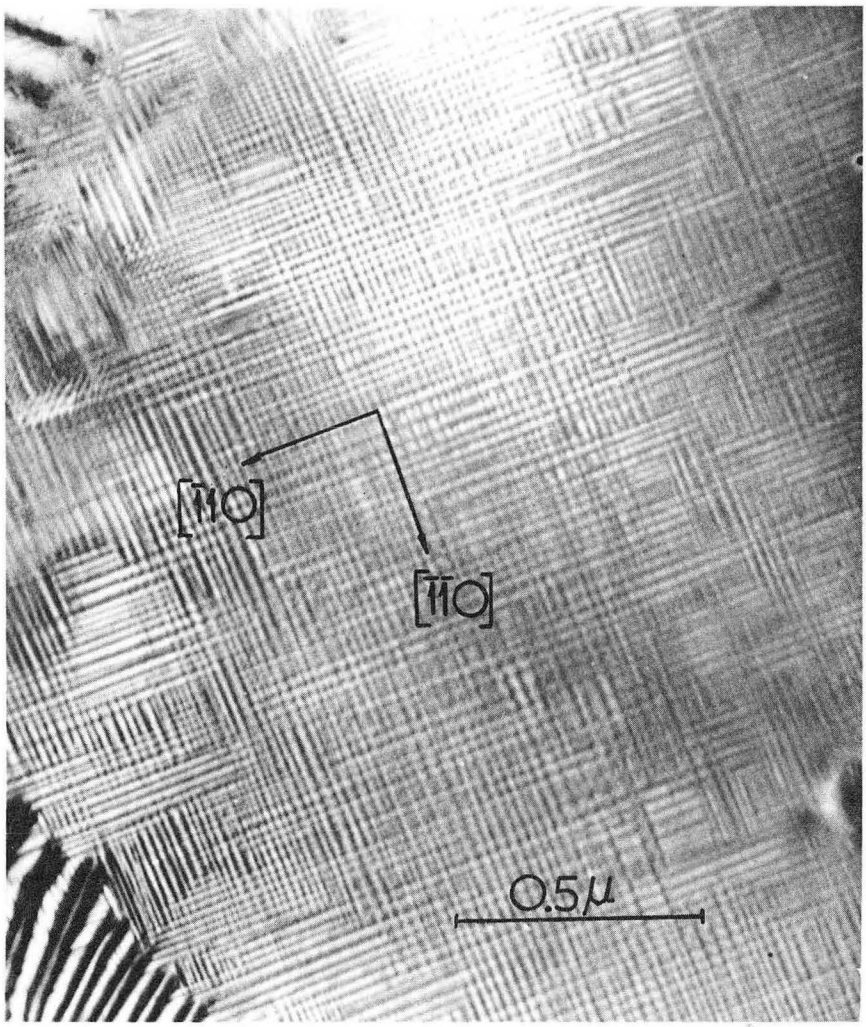

ZN-4717

Fig. 2

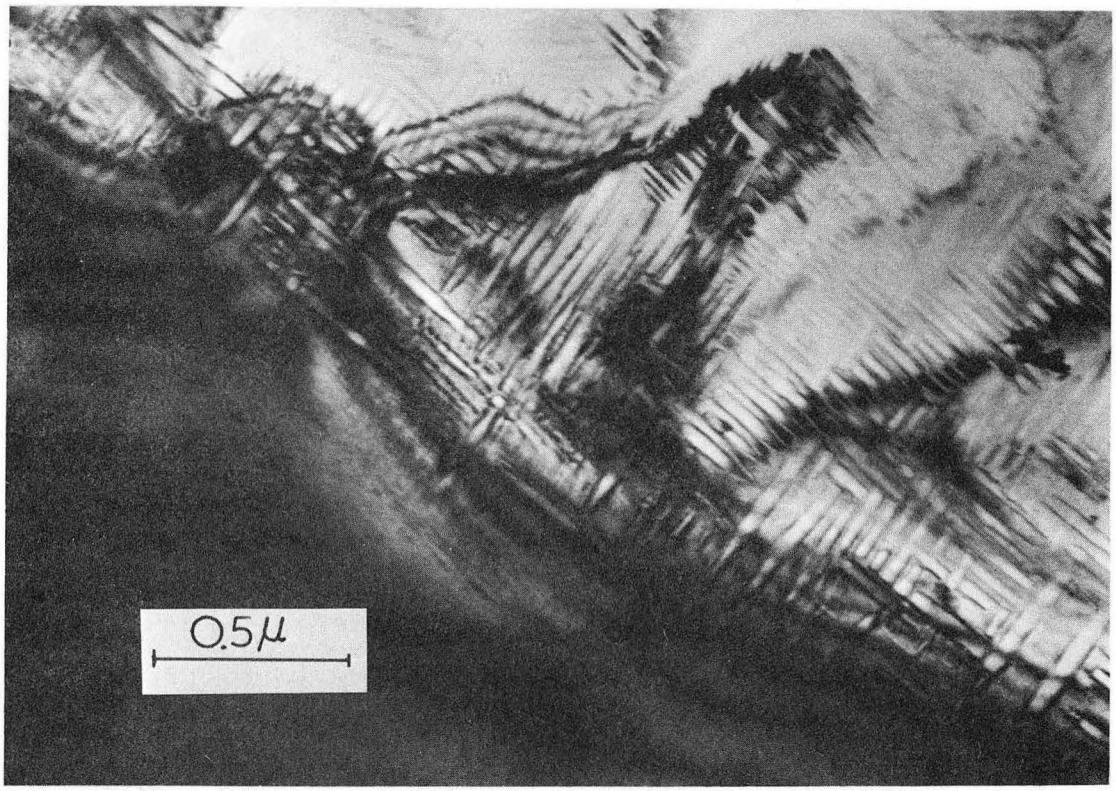

ZN-4718

Fig. 3

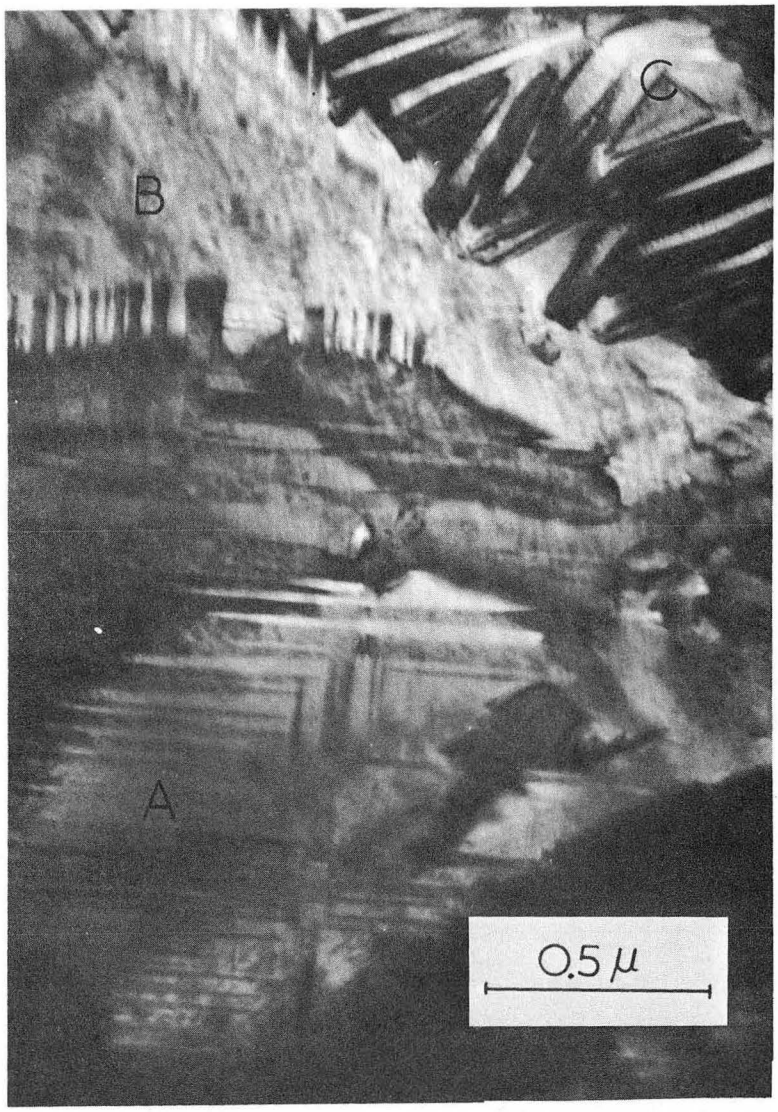

ZN-4719

Fig. 4

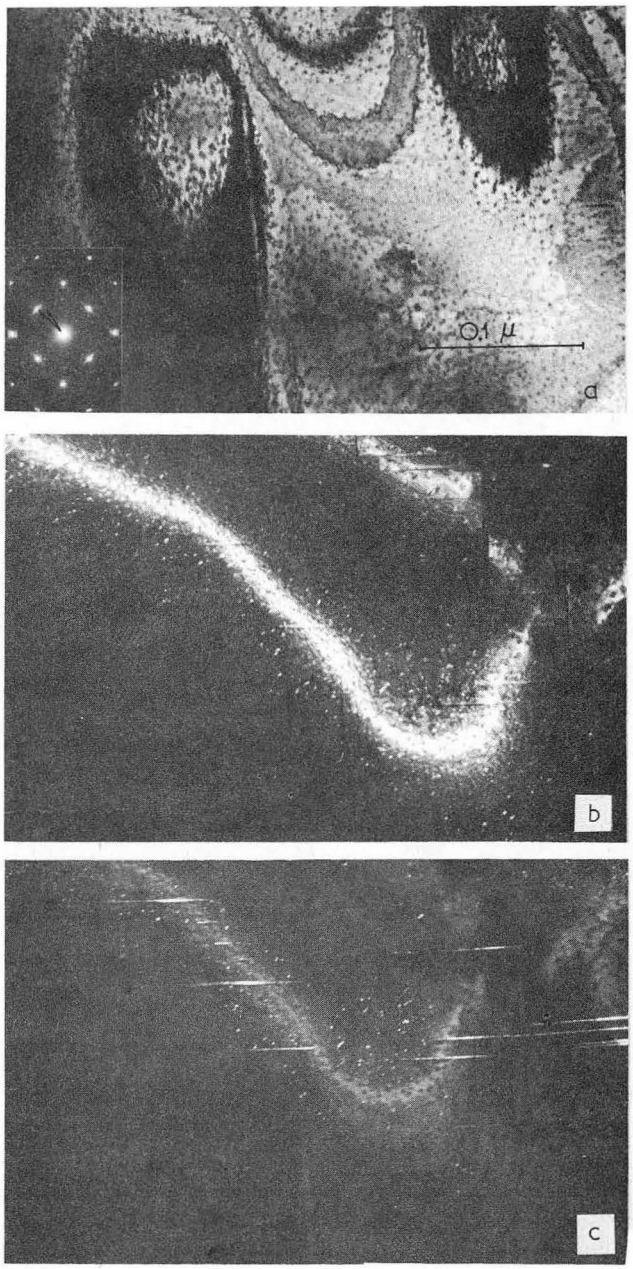

ZN-4720

Fig. 5

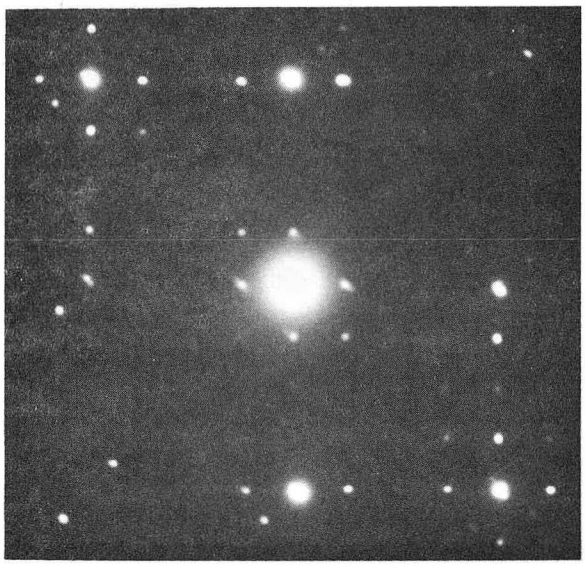

a

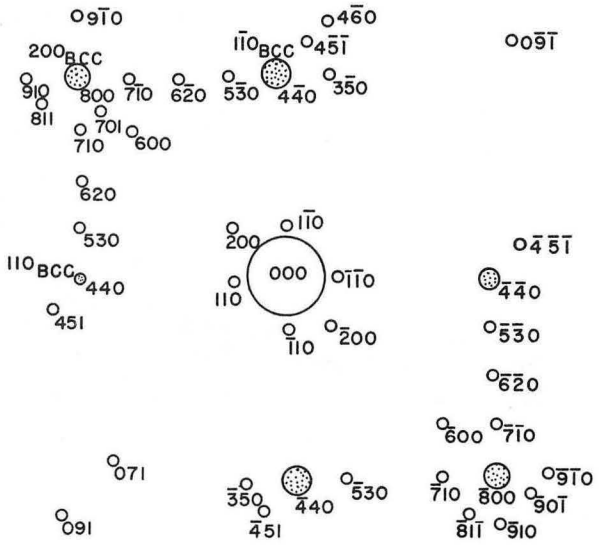

ZN-4653

b

Fig. 6

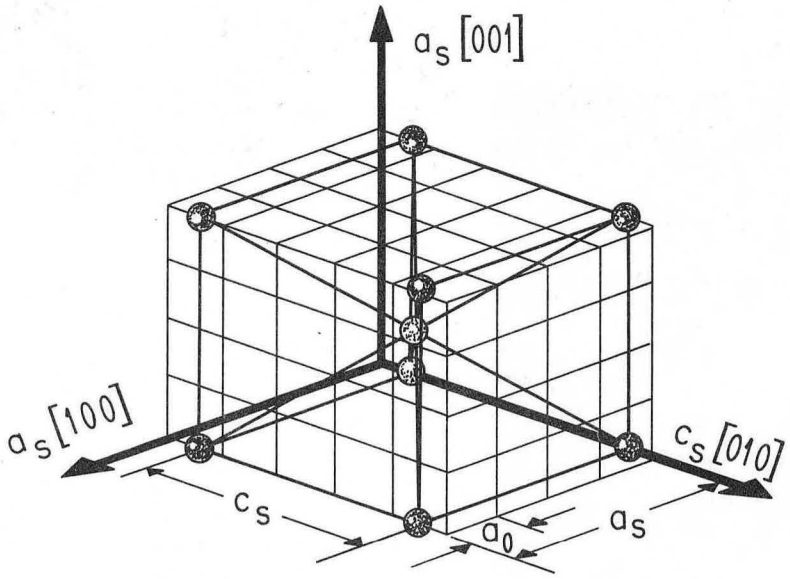

MU-35009

Fig. 7

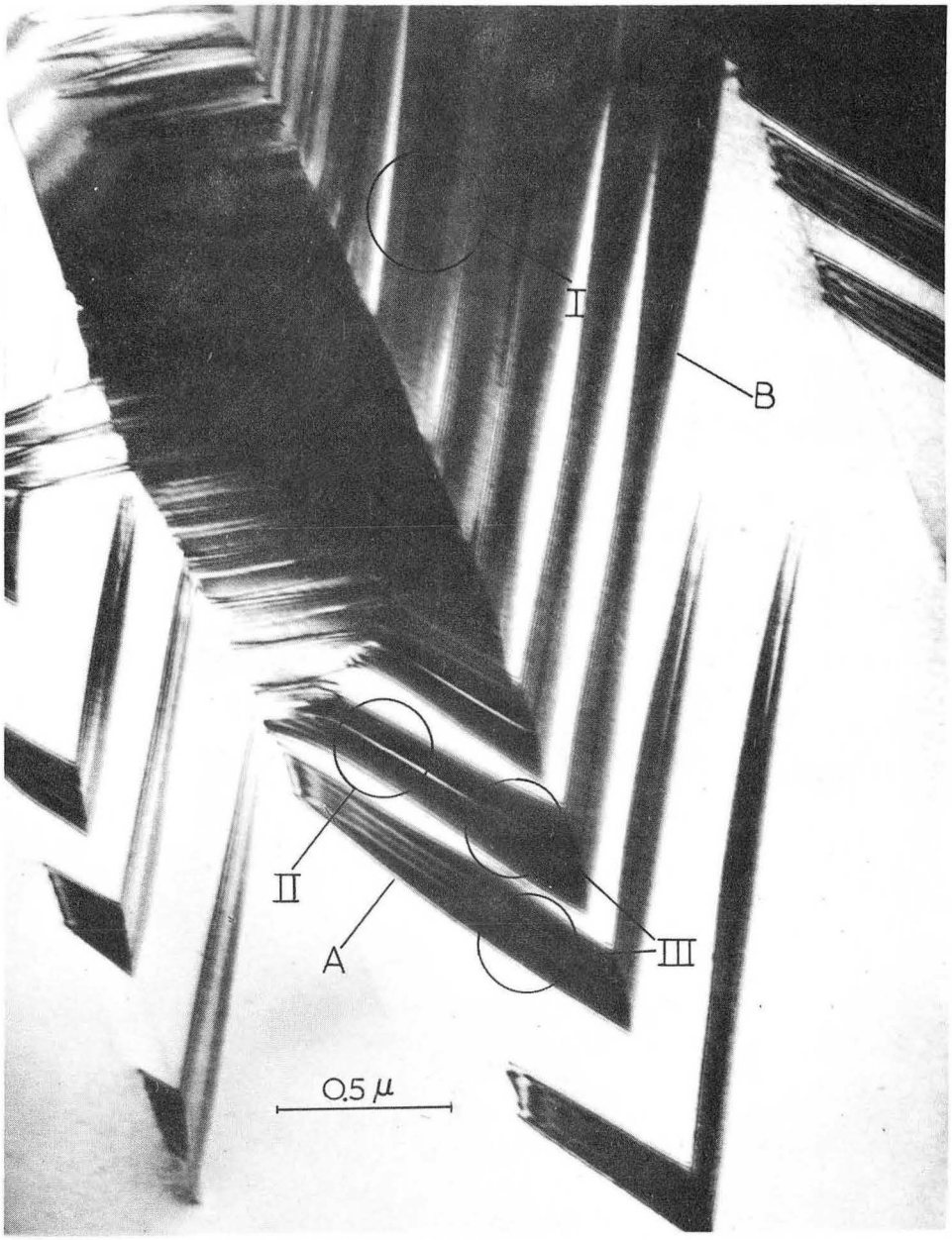

ZN-4721

Fig. 8

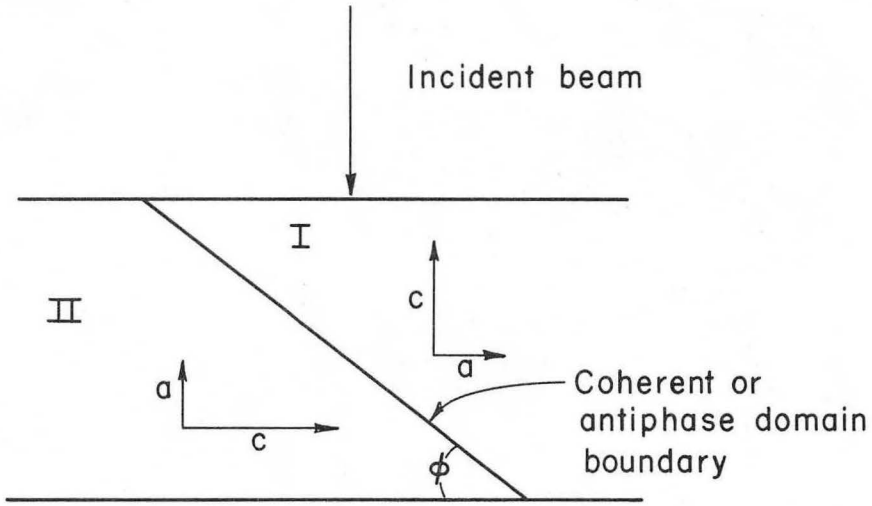

MU-35008

Fig. 9

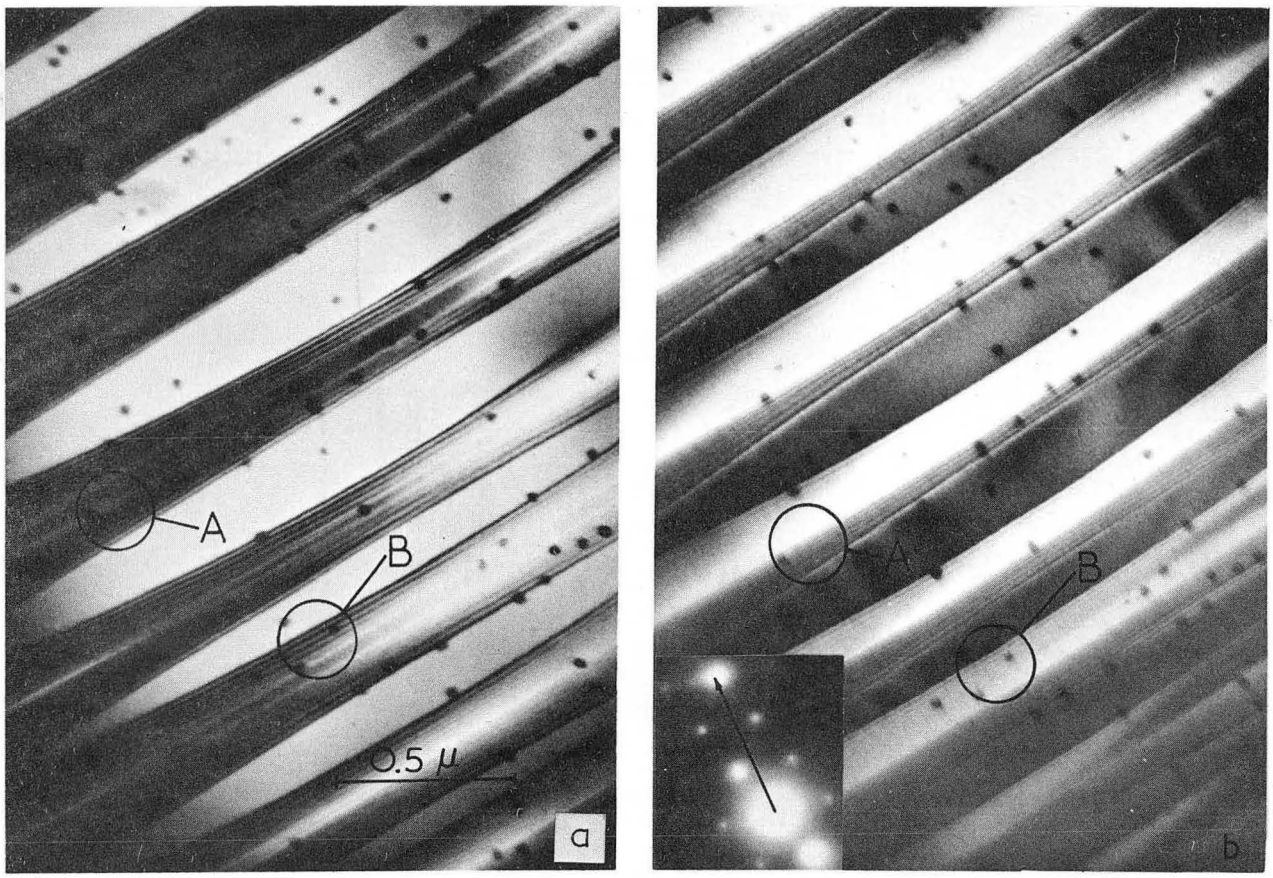

ZN-4722

Fig. 10

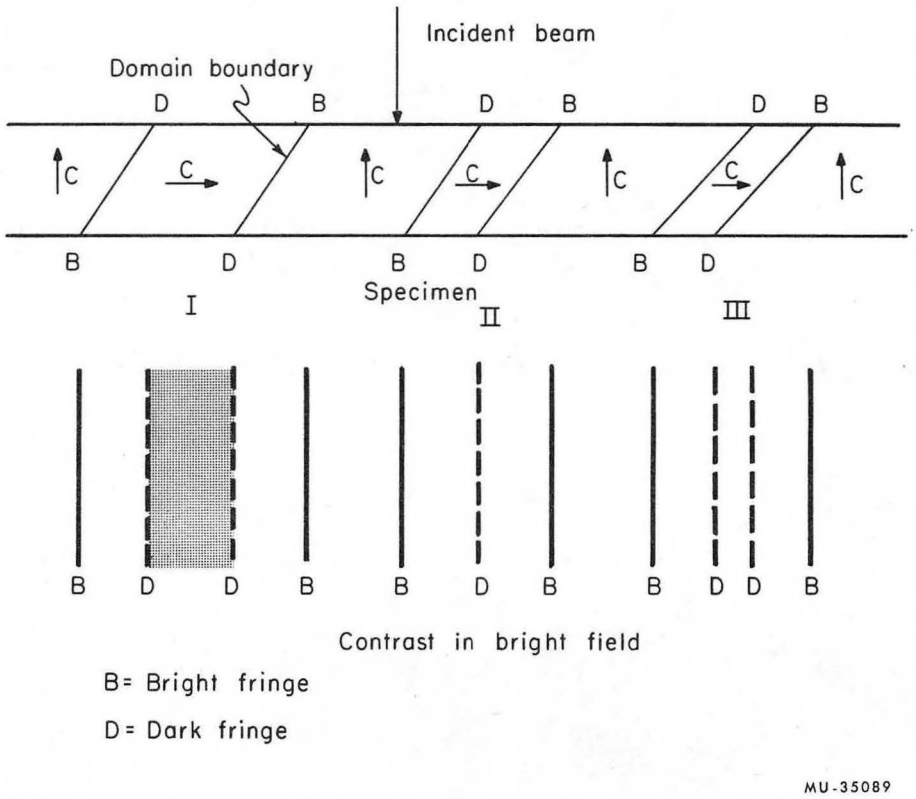
Incident beam
Domain boundary
D B D B D B
C C C C C C
B D B D B D
Specimen
I
II
III
B D D B B D B B D D B
Contrast in bright field
B= Bright fringe
D= Dark fringe
MU-35089

Fig. 11

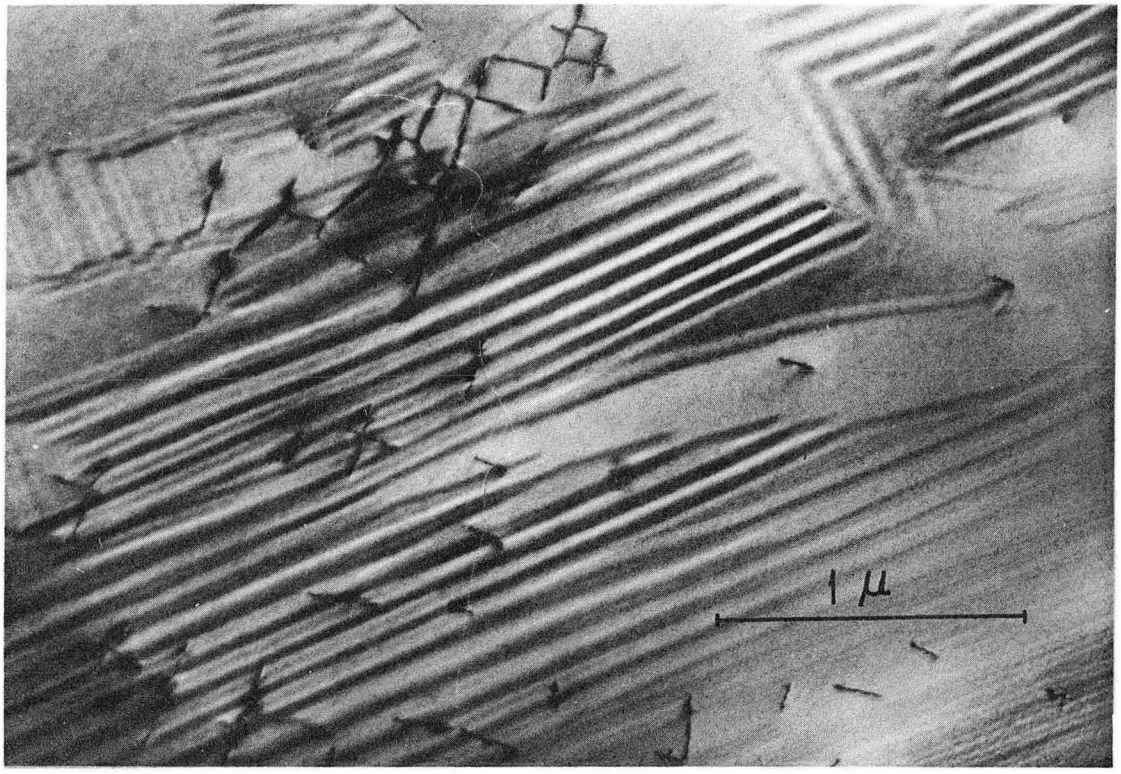

ZN-4723

Fig. 12

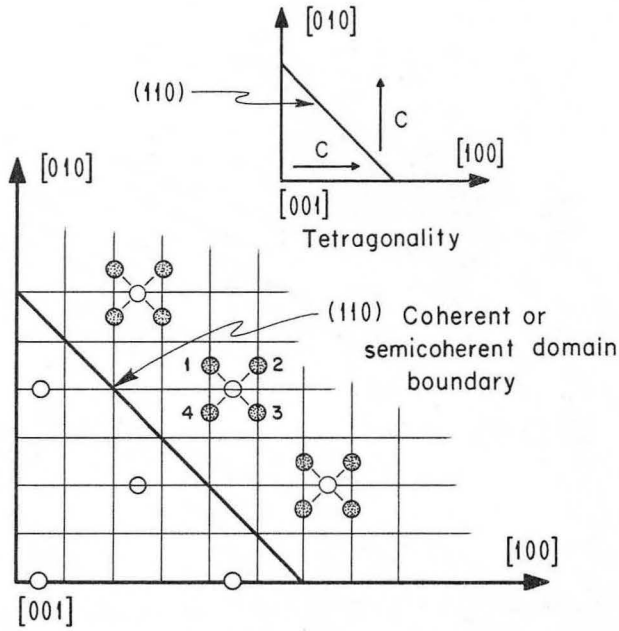
[010]
(110)
C
C
[100]
[001]
Tetragonality
[010]
(110) Coherent or
semicoherent domain
boundary
1
2
4
3
[100]
[001]
MU-35088

Fig. 13

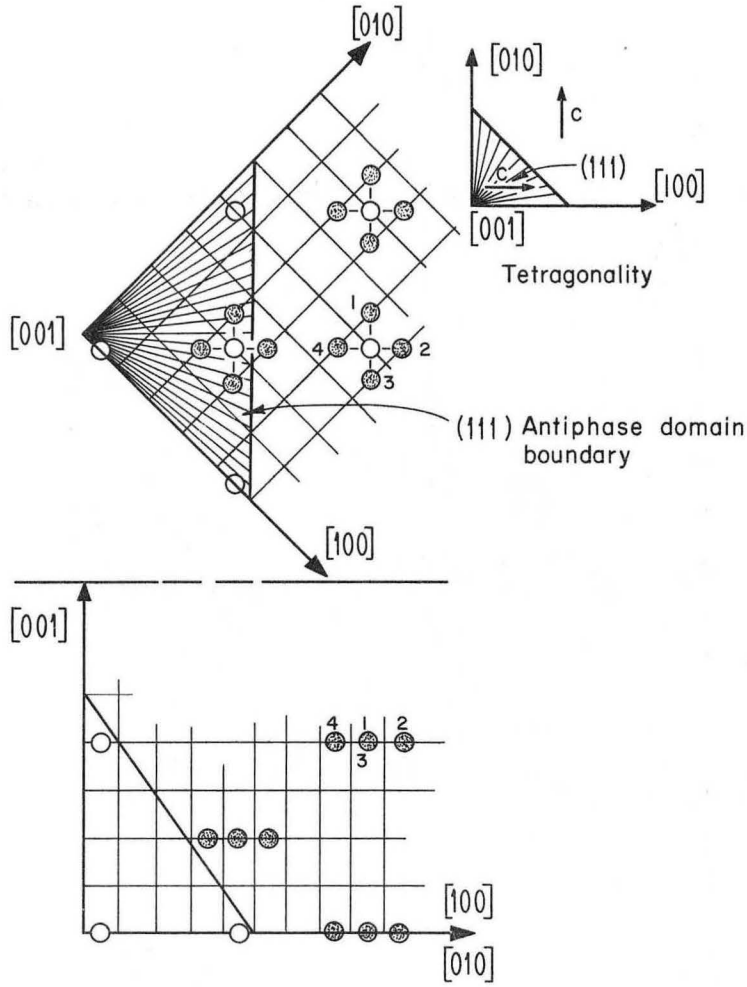
[010]
[010]
c
(111)
[100]
[001]
Tetragonality
[001]
1
4
2
3
(111) Antiphase domain boundary
[100]
[001]
4
1
2
3
[100]
[010]
MU-35010

Fig. 14

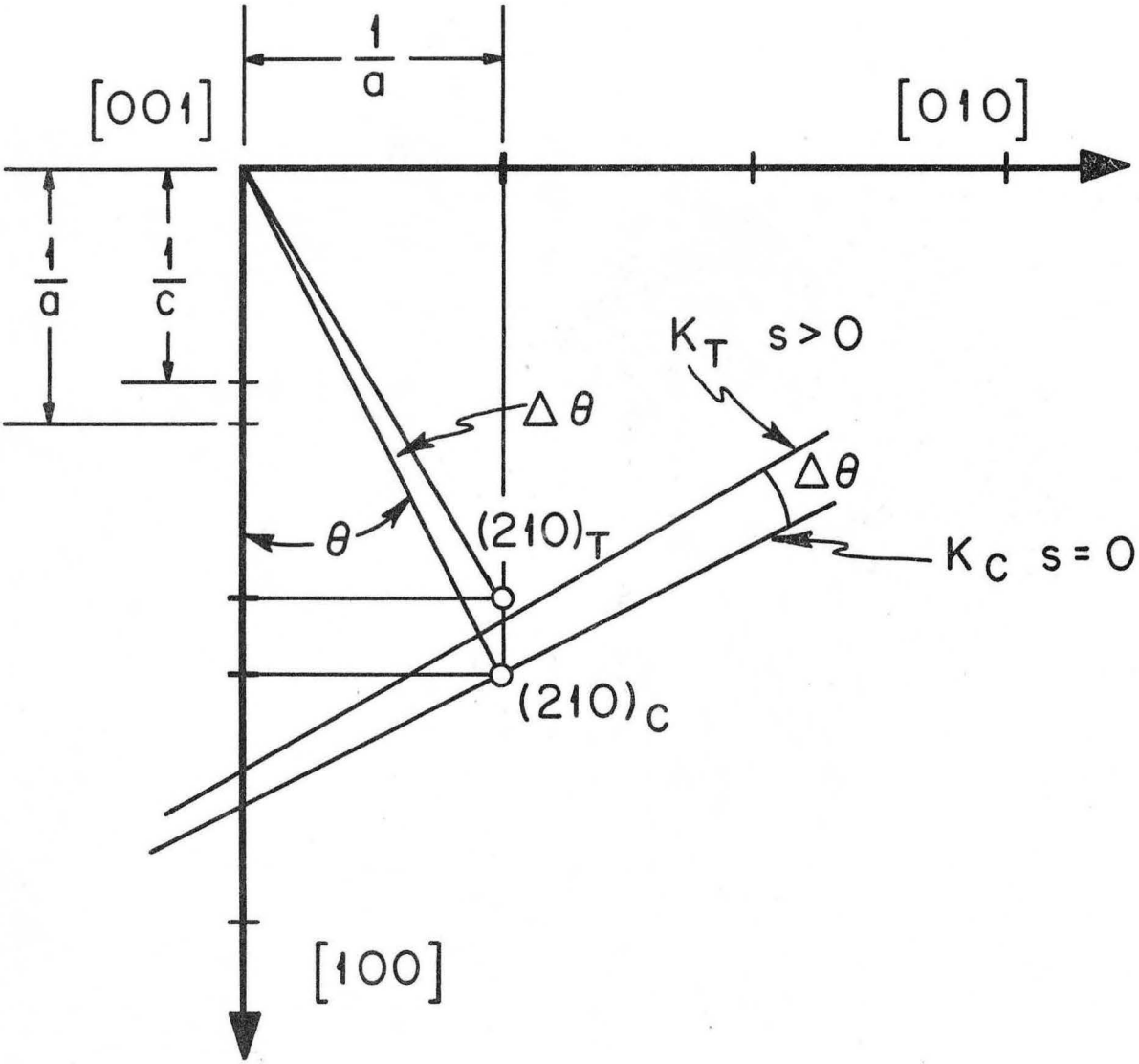

MUB-4582

Fig. 15

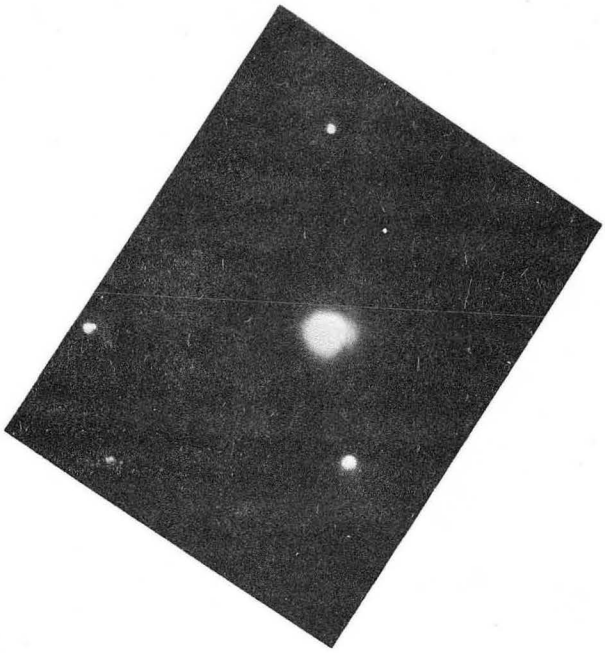

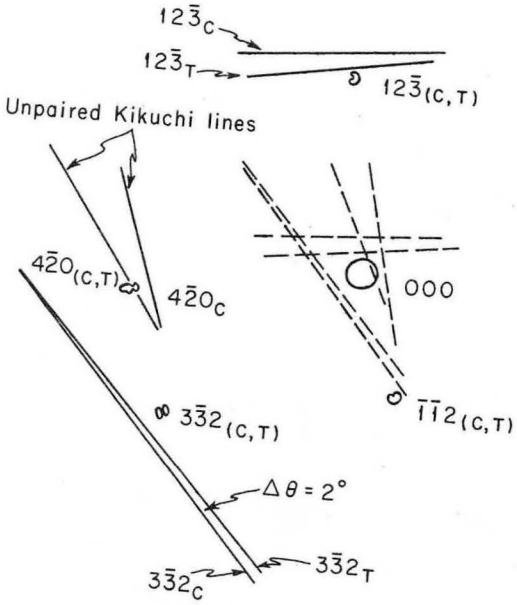

ZN-4595

a

b

Fig. 16

This report was prepared as an account of Government sponsored work. Neither the United States, nor the Commission, nor any person acting on behalf of the Commission:

A. Makes any warranty or representation, expressed or implied, with respect to the accuracy, completeness, or usefulness of the information contained in this report, or that the use of any information, apparatus, method, or process disclosed in this report may not infringe privately owned rights; or

B. Assumes any liabilities with respect to the use of, or for damages resulting from the use of any information, apparatus, method, or process disclosed in this report.

As used in the above, "person acting on behalf of the Commission" includes any employee or contractor of the Commission, or employee of such contractor, to the extent that such employee or contractor of the Commission, or employee of such contractor prepares, disseminates, or provides access to, any information pursuant to his employment or contract with the Commission, or his employment with such contractor.